

## Power Exhaust on JET: an Overview of Dedicated Experiments

W.Fundamenski, P.Andrew, T.Eich<sup>1</sup>, G.F.Matthews, R.A.Pitts<sup>2</sup>, V.Riccardo, W.Sailer<sup>3</sup>, S.Sipilä<sup>4</sup> and JET EFDA contributors\*

*Euratom/UKAEA Fusion Association, Culham Science Centre, Abingdon, OX14 3DB, UK*

<sup>1</sup>*Max-Planck-Institut für Plasmaphysik, Euratom Assoc., D-85478, Garching, Germany*

<sup>2</sup>*CRPP, Assoc. Euratom-CSEPF, CH-1015, Lausanne, Switzerland*

<sup>3</sup>*Universität Innsbruck, Technikerstraße 25, A-6020 Innsbruck, Austria*

<sup>4</sup>*Helsinki U. of Technology, Tekes-Euratom Assoc., PO Box 2200, FIN-02015 HUT, Finland*

**Abstract:** Energy transport in the SOL was studied for a variety of JET plasmas with an emphasis on Type-I ELMy H-mode. Under ITER relevant, low collisionality conditions, inter-ELM radial energy transport was found to be dominated by (neo-)classical ion conduction, i.e. by diffusion of heat due to ion-ion collisions. The radial convection of the ELM filaments with  $\langle v_{\perp} \rangle \sim 0.6 \pm 0.3$  km/s,  $\langle v_{\perp} / c_s \rangle \sim 0.2$  % and  $\langle v_{\perp} \rangle / \langle c_s \rangle \sim 0.3 \pm 0.1$  % agrees well with a sheath-limited model of plasmoid propagation. Within the filament, the electrons are cooled more rapidly than the ions, which retain much of their initial energy when striking the outboard limiter.

### 1. Introduction

The exhaust of power from the core plasma via the scrape-off layer (SOL) and the associated energy fluxes on divertor plates and main chamber limiters, are critical issues for ITER [1]. Characterisation of power deposition profiles and inferences about SOL energy transport mechanisms are thus high priority tasks for the ITER project. The absence of a credible theory for the radial heat diffusivity  $\chi_{\perp}^{\text{SOL}}$ , especially its functional dependence on local *field* and *plasma* variables, was considered in the ITER Physics Basis [2] to be the weakest link in the predictive chain, preventing a true coupling of code and theory, and reducing ITER extrapolation to empirical power width  $\lambda_q$  scalings. The above assessment motivated a series of JET experiments during the past years dedicated to the study of power exhaust aimed at characterising both inter-ELM and ELM transport in the parallel, diamagnetic and radial  $\{\parallel, \wedge \text{ and } \perp\}$  directions, evolving naturally out of the work reported on at the previous IAEA conference [3].

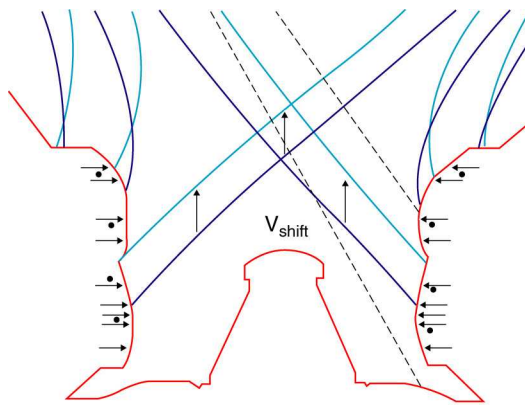


Figure 1: Divertor diagnostics and vertical sweep equilibrium

A standard, high clearance magnetic configuration was adopted for these experiments, its main advantage being the freedom to slowly shift the plasma as a rigid-body, either vertically or radially [3-5]. All plasmas had identical shape (boundary elongation  $\sim 1.7$ , triangularity  $\delta_U = 0.16$ ,  $\delta_L = 0.24$ , wall clearance  $\Delta R_{\text{in}} = 26$  cm,  $\Delta R_{\text{out}} = 16$  cm). Vertical translation was employed to characterise the deposited power profiles on the inner and outer divertors using Langmuir probes (LP), infrared thermography (IR) and embedded thermocouples (TC), Fig.1 [4,5]. A fair agreement between the profile shape measured by the three diagnostics has been shown in both L- and H-modes; a detailed discussion

may be found in Refr. [9]. Sweeps in both directions were used to measure the radial interaction of ELMs with outboard limiters using limiter Langmuir probes, fast magnetics, visible spectroscopy, soft X-ray and target IR camera diagnostics. Three types of scans were employed: a) mass of plasma ions: D, He, (or charge, since  $A/Z = 2$ ), b) magnetic field and plasma current:  $B_t \sim 1-3$  T,  $q_{95} \sim 2.6-3.8$ ,  $B_t$  direction, c) heating power (4-18 MW) and fuelling rate ( $n/n_{\text{GW}} \sim 0.3-1$ ). This article deals exclusively with vertical sweep experiments.

### 2. Inter-ELM Transport

#### 2.1 Forward field (fwd-B) experiments: $B \times \nabla B$ towards the divertor

Over the past years, 22 dedicated discharges were performed on JET in the standard high clearance configuration in the forward field direction for a variety of heating powers and plasma densities, in both deuterium and helium (16 D, 6 He), and both confinement regimes (3 L-modes, 19 H-modes) [9].

Time-averaged total power deposition profiles were obtained for each of the above discharges using the swept strike-point TC technique, while electron power profiles were measured using the divertor LP array. The profiles are parameterised in terms of two variables: peak heat flux  $q_0$  and the integral width, defined as  $\lambda_q \equiv \int q dr / q_0$ . All heat fluxes are expressed as wall loads, i.e. per unit area of the divertor target; heat fluxes  $\parallel$  to the magnetic field are related to target fluxes by  $q_{\parallel}/q_t \sim 1/\sin\theta_{\perp}$ , where  $\theta_{\perp} \sim 3-5^\circ$  is the field line angle relative to the target. Profile widths are mapped from the target to the outer mid-plane (omp) or upstream location using  $\lambda_q[\text{omp}] = \lambda_q[z]/\Phi$ , where  $\Phi \sim 4$  is the flux expansion factor obtained from EFIT reconstruction.

The separatrix collisionality ( $\nu_i^* \equiv L_{\parallel}/\lambda_{ii} \sim L_{\parallel}n/T_i^2$ ) with  $L_{\parallel}$  the connection length, emerges as the governing parameter. For high power, natural density H-modes ( $\nu_i^* < 5$ ), the peak heat flux on the outer divertor  $q_{\text{tot}}$  exceeds the electron heat flux  $q_e$ , which we interpret as an ion contribution  $q_i \sim q_{\text{tot}} - q_e$ , since charge exchange neutrals and radiation are far too small to explain the excess energy, Fig.2&3. For lower power, higher density or higher ion charge ( $\nu_i^* > 10$ ), the electron power dominates ( $q_{\text{tot}}/q_e = q_{\text{TC}}/q_{\text{LP}} \sim 7/5$  where  $q_{\text{LP}} = 5T_e\Gamma_e$ ) as expected from sheath physics, Fig.2&3. The above holds for both D and He plasmas over a large range of powers, densities, fields and currents. This outer target ion contribution  $q_i$  is closely correlated with the narrow structure (NS) in the power profile, which we measure as the near-SOL peak power,  $q_{\text{NS}} \sim q_{\text{tot}} - q_{\text{base}}$ , where  $q_{\text{base}}$  is the peak power extrapolated from the far-SOL (base) profile to the separatrix, Fig.3. Peak powers are smaller by a factor of five at the inner target; this level of asymmetry can not be explained by geometry and ballooning-like transport alone, suggesting that classical drift effects are responsible.

The inferred  $T_i^{\text{D}^+}$  for  $\text{D}^+$  ions striking the outer target is  $\sim 300$  eV at  $\nu_i^* \sim 1$ , while the CXRS measured  $T_i^{\text{C}6^+}$  profiles indicate that  $T_i^{\text{C}6^+}$  varies slowly in the pedestal region, with  $T_{i,\text{sep}}^{\text{C}6^+} \sim 0.8T_{i,\text{ped}}^{\text{C}6^+} \sim 700$  eV [11]. Assuming  $T_i^{\text{D}^+}/T_i^{\text{C}6^+} > 0.5$ , this suggests that 'hot' target ions originate inside the pedestal region (within  $\sim \rho_{\theta i}$  of the separatrix) suggesting ion orbit loss (IOL) or neo-classical ion effects in general [6,7]. Although electrons remain collisional ( $\nu_e^* \sim 25$ ) in all cases considered, they are only weakly thermally coupled to the ions ( $\nu_{ie}^* \sim 0.5$ ) in the main SOL, which partly explains the different scaling of electron and ion power profiles for  $\nu_i^* < 5$ . Narrow outer target profiles ( $\lambda_q \sim 3-5\rho_i$ ) were observed in the near-SOL, in low collisionality ( $\nu_i^* < 5$ ) H-modes, with the integral power width found to scale according to

$$\lambda_q^{\text{H}} \propto A(Z)B_{\phi}^{-1}q_{95}^{0.6}P_t^{-0.4}n_{e,u}^{0.25} \quad (1)$$

Comparison of (1) with the predictions from all available theories of  $\chi_{\perp}^{\text{SOL}}$ , indicates that classical ion conduction **A1** gives the best match to the data, followed by neo-classical ion conduction **A2** and classical electron conduction **A3**, Fig.4, which plots the difference between scaling exponents of (1)

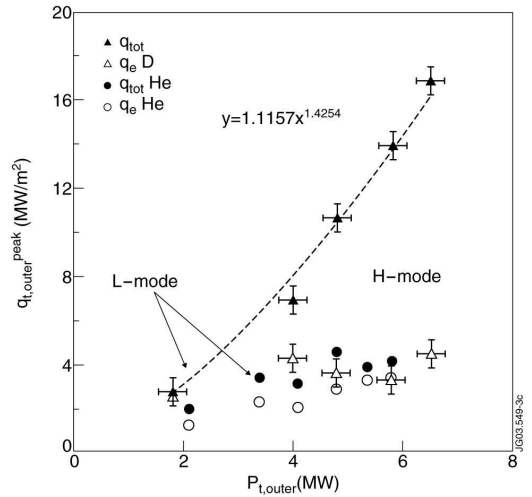


Figure 2: peak heat fluxes vs. target power

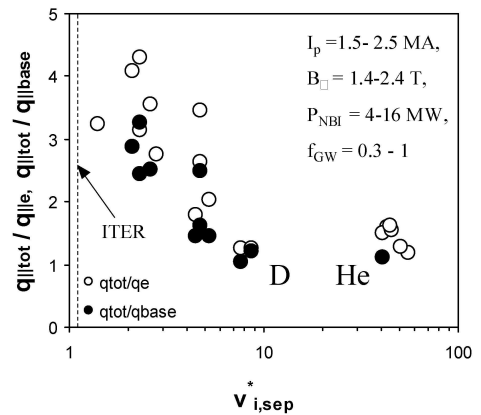


Figure 3: Ion contribution and narrow structure at low collisionality

and theoretical predictions of the same, where letters denote different theories. **A1** is a clear favourite if only the well know quantities  $Z(A)$ ,  $B$ ,  $q_{95}$  are considered. It is also the only theory to satisfy the error margin indicated by the dot-dashed line in Fig.4. Based on LP measured electron power width  $\lambda_q^e$  scaling, **A1** is the second best model. Similar comparison based on IR measured  $\lambda_q^{\text{tot}}$  scaling (D only) with  $q_{95}$ ,  $\langle n_e \rangle$  and  $T_\sigma$ , points to MHD interchange (**B,C,E**) and classical transport (**A1-A3**) [9]. The magnitude of  $\lambda_q^{\text{TC}}$  lies between classical **A1** and neo-classical **A2** predictions,  $\lambda_q^{\text{TC}} \sim 2.24\lambda_q^{\text{A1}} \sim 0.27\lambda_q^{\text{A2}}$ , where  $\lambda_q^\Psi = (\chi_\perp^\Psi L_\parallel / Mc_s)^{1/2}$  is the power width for theory  $\Psi$  and  $M \sim 1$  was assumed (for  $M \sim 0.2$ , we find  $\lambda_q^{\text{TC}} \sim \lambda_q^{\text{A1}}$ ). It is well matched by transitional estimates,  $\lambda_q^{\text{IOL-v}^*} = \lambda_q^{\text{IOL}} v_i^{*1/2}$  and  $\lambda_q^{\text{A1-IOL}} = 2.4\zeta\lambda_q^{\text{A1}} + (1-\zeta)\lambda_q^{\text{IOL}}$ , where  $\zeta \equiv v_i^* / (1 + v_i^*)$  and

$$\lambda_q^{\text{IOL}} = 2.2 \times 10^{-3} A^{0.35 \pm 0.03} Z^{-0.8 \pm 0.06} B_\phi^{-0.89 \pm 0.04} q_{95}^{0.88 \pm 0.04} (R/3)^{0.8 \pm 0.1} \quad (2)$$

with  $B_\phi$  in T, and  $R$  and  $\lambda_q$  in m [9]. The result (2) was found using the guiding centre Monte-Carlo code ASCOT, used to simulate ion orbit loss in realistic JET magnetic geometry [6,7,16]. This prediction is broadly consistent with  $\chi_\perp^i \sim (1-5)\chi_\perp^{\text{A1}}$ , although IOL is a non-diffusive process.

It thus appears that  $\perp$  (radial) electron energy transport is anomalous ( $\lambda_{qe} \sim \lambda_q \sim 60-200\rho_e$ ) most likely governed by electrostatic turbulence driven by interchange modes and drift-wave instabilities (as suggested by AUG studies) [10,12], while  $\perp$  ion energy transport is governed by (neo-)classical ion conduction. The contribution of IOL remains unclear, with ASCOT simulations suggesting that the observed profiles can be reconciled with IOL provided rather large values of the radial electric field are assumed in the SOL ( $E_r^{\text{SOL}} \sim 30-50$  kV/m), eg. modelling correctly predicts  $v_i^*$  as the main ordering parameter. However, the predicted IOL target profile  $\lambda_q^{\text{IOL}} \sim \rho_{\theta,i}$  is in poor agreement with the observed scalings with  $A(Z)$ ,  $B_\phi$  and  $q_{95}$ .

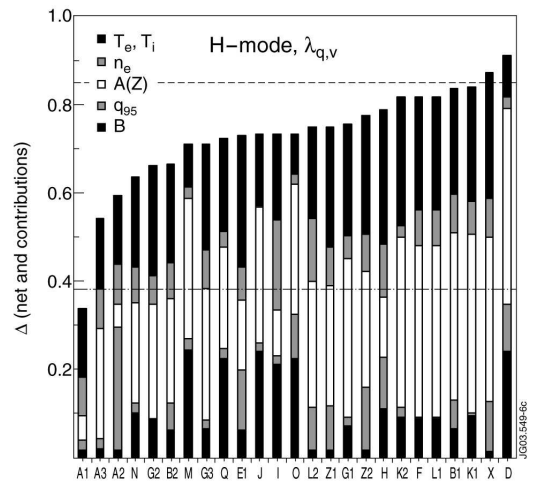


Figure 4: difference between theory and experiment for all published theories

## 2.2 Reversed field (rev-B) experiments: $B \times \nabla B$ away from the divertor

In order to discriminate between the two candidate theories consistent with observed fwd-B data (IOL and neo-classical ion conduction – only the former being sensitive to the  $B \times \nabla B$  direction) dedicated reversed field experiments were recently carried out on JET [13,14]. Four good discharges, forming fwd-B/rev-B matched pairs were obtained (one L-mode and three H-modes at different values of  $B_\phi$ ,  $I_p$  and  $P_{\text{heat}}$ ). The out-in peak heat flux asymmetry (both TC and LP) ranges from 5-7 for fwd-B, and 1.7-3.7 for rev-B. The ratio of total to electron power in H-mode is smaller for fwd-B than for rev-B, 2-5 vs. 1.2-1.8, respectively. The average out-in power asymmetry of both target  $P_t$  and divertor  $P_{\text{div}}$  powers increases roughly linearly with power into the SOL,  $P_{\text{SOL}}$ .

The TC-measured peak heat flux values were plotted vs. the scaling  $q_t \sim P_t/\lambda_q$  with  $\lambda_q$ , given by (1), derived from two dozen outer target fwd-B shots (mostly H-modes), Fig.5. Within the measurement errors, the outer target rev-B H-mode points do not substantially differ from the fwd-B scaling, while the inner and L-modes points are only grossly correlated with the scaling. We conclude that under low collisionality (attached) conditions, the power width  $\lambda_q$  is insensitive to the  $B \times \nabla B$  direction. Since this

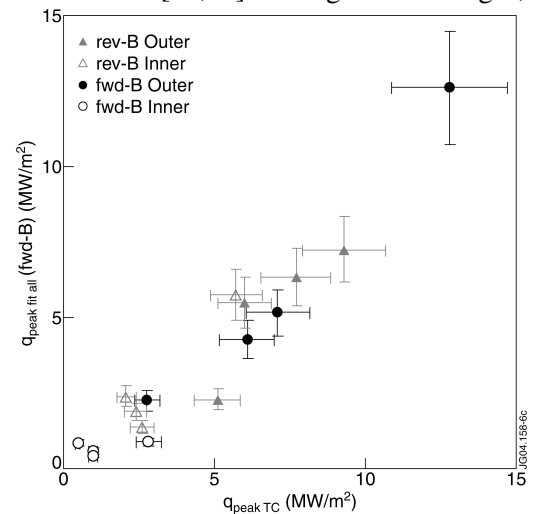


Figure 5: rev-B data follows the fwd-B scaling

quantity is directly related to the radial ( $\perp$ ) heat diffusivity,  $\lambda_q \sim (\chi_{\perp} \tau_{\parallel})^{1/2}$ , we may infer that radial energy transport in the SOL is largely *independent* of the  $\mathbf{B} \times \nabla B$  direction, hence of classical drift effects, i.e. the  $\mathbf{B} \times \nabla B$  direction affects the poloidal ( $\theta$ ) but not the radial ( $\perp$ ) energy transport. The former observation suggests the role of classical drifts which for ITER relevant, low collisionality ( $v_i^* < 5$ ) plasmas, lie pre-dominantly on flux surfaces, pointing in the diamagnetic ( $\wedge$ ) direction, and whose sign is determined by the toroidal field direction and which largely determine SOL flows (both main species and impurity) and divertor asymmetries (density, temperature, pressure, power and radiation). In order to predict the latter, we note that the majority of the power enters the SOL on the low field side (LFS), irrespective of the  $\mathbf{B} \times \nabla B$  direction, as a consequence of: a) geometry (larger outboard area), b) Shafranov shift compressing the flux surfaces on LFS, c) bad curvature and the consequent increase in MHD-turbulence on LFS. These effects together with  $R_o/R_i \sim L_{\parallel i}/L_{\parallel o} \sim 2$  predict an average out-in power asymmetry of  $\sim 2$  (1.7 due to surface area alone) in rough agreement with experiment. To improve this prediction, we consider the drift related fluxes in the SOL [15],

$$\mathbf{q}_{\sigma} \approx 2.5 p_{\sigma} \mathbf{v}_{\sigma} + 2.5 p_{\sigma} v_{t\sigma} \rho_{\sigma} \mathbf{b} \times \nabla T_{\sigma} / T_{\sigma} \quad (3)$$

$$\mathbf{v}_{\sigma} = v_{\parallel\sigma} \mathbf{b} + \mathbf{v}^E + \mathbf{b} \times (\nabla p_{\perp\sigma} - \mathbf{R}) / m_{\sigma} n_{\sigma} \Omega_{\sigma} + \{ (v_{\parallel\sigma}^2 - v_{\perp\sigma}^2 + v_{\parallel\sigma}^2) / \Omega_{\sigma} \} \mathbf{b} \times \mathbf{b} \cdot \nabla \mathbf{b}$$

where  $\mathbf{b} = \mathbf{B}/B$  is a unit vector,  $\mathbf{v}^E \sim (1+0.25\rho_{\sigma}^2 \nabla^2) \mathbf{E} \times \mathbf{b} / B \sim \mathbf{E} \times \mathbf{b} / B$  is the electrostatic drift velocity,  $v_{\parallel\sigma} = (T_{\parallel\sigma} / m_{\sigma})^{1/2}$  and  $v_{\perp\sigma} = (T_{\perp\sigma} / m_{\sigma})^{1/2}$  are thermal velocities,  $p_{\sigma} = n T_{\sigma}$  is the static pressure,  $\Omega_{\sigma} = e_{\sigma} B / m_{\sigma}$  is the gyro-frequency,  $\rho_{\sigma} = v_{\perp\sigma} / \Omega_{\sigma} \sim v_{t\sigma} / \Omega_{\sigma}$  the thermal gyro-radius,  $\sigma \in \{i, e\}$  the species index,  $e_{\sigma}$  is the charge ( $-e$  for electrons,  $+Ze$  for ions). Dominant contributions to the  $\theta$  (strictly speaking  $\wedge$ ) components of (1) arise due to  $\mathbf{E} \times \mathbf{B}$  and diamagnetic drifts. We write these explicitly as,

$$q_{\sigma\wedge}^E \sim 2.5 p_{\sigma} E_{\perp} / B_{\theta}, \quad q_{\sigma\wedge}^{\nabla p} \sim 2.5 (T_{\sigma} / e_{\sigma} B_{\theta}) \nabla_{\perp} p_{\perp\sigma}, \quad q_{\sigma\wedge}^{\nabla T} \sim 2.5 (p_{\sigma} / e_{\sigma} B_{\theta}) \nabla_{\perp} T_{\sigma} \quad (4)$$

To first order, we can estimate the radial E-field as  $E_{\perp} \sim 3 \nabla_{\perp} T_{e,t}$  evaluated at the outer target. Writing the  $\theta$  component of the  $\parallel$  energy flux as  $q_{\theta\sigma} = (B_{\theta} / B) q_{\parallel\sigma}$  with  $q_{\parallel\sigma} \sim p_{\sigma} L_{\parallel} / \tau_{\parallel\sigma}$  and  $\tau_{\parallel i} \sim L_{\parallel} / c_s$ ,  $\tau_{\parallel e} \sim L_{\parallel}^2 / \chi_{\parallel e}$ , we find

$$q_{i\theta}^E / q_{i\theta} \sim 3 \nabla_{\perp} T_{e,t} / c_s B_{\theta} \sim 3 \rho_{\theta s} / \lambda_{Te,t}, \quad q_{e\theta}^E / q_{e\theta} \sim v_{e\theta}^* \rho_{\theta s} / \lambda_{Te,t} \quad (5)$$

$$q_{i\theta}^{\nabla T} / q_{i\theta} \sim \nabla_{\perp} T_{\sigma,t} / c_s e_{\sigma} B_{\theta} \sim \pm \rho_{\theta s} / \lambda_{Ti}, \quad q_{e\theta}^{\nabla T} / q_{e\theta} \sim v_{e\theta}^* \rho_{\theta s} / \lambda_{Te}$$

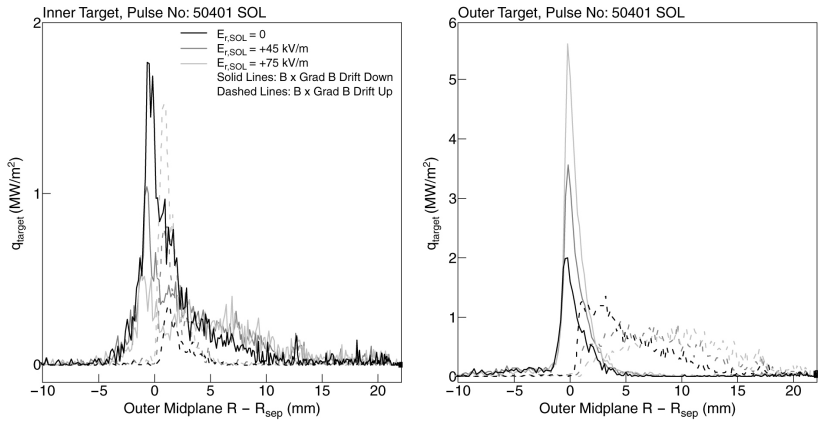


Figure 6: ASCOT simulated IOL target power profiles, fwd-B vs. rev-B

for low  $v_i^*$ . Using the experimental  $\lambda_q$  (1) as a rough guide for the  $\lambda_{T\sigma}$  scaling, we find that the B-dependence cancels, leaving a positive, roughly linear, power scaling,

$$\{q_{\sigma\wedge}^E, q_{\sigma\wedge}^{\nabla T}\} / q_{\sigma\wedge} \propto T_{\sigma,t}^{0.5} P_{SOL}^{0.5} n_{e,u}^{-0.2} \quad (6)$$

in agreement with experiment [13,14]. This strongly suggests that the out-in divertor energy asymmetries are a direct consequence of classical ( $\mathbf{E} \times \mathbf{B}$  and/or  $\mathbf{B} \times \nabla T_i$ ) drift-related heat fluxes in the

where  $c_s = \{(ZT_e + T_i) / m_i\}^{1/2}$  is the plasma sound speed. Hence the ratio of the poloidal components of the drift and parallel heat fluxes can be estimated as the gyro-radius normalised by the temperature gradient length,  $\lambda_{T\sigma} \equiv |\nabla_{\perp} T_{\sigma} / T_{\sigma}|^{-1}$ . Since  $\lambda_q \sim 3-5\rho_i \sim 0.3-0.5\rho_{\theta i}$  in high power H-modes on JET, with typical  $\lambda_{T\sigma} \sim 2-3\lambda_q$ , we can expect  $\rho_{\theta i} / \lambda_{Ti} \sim O(1)$  and thus a significant contribution from drift effects

SOL. This prediction has been largely confirmed by numerical simulations using the EDGE2D transport code in which classical drift effects have been included [14].

The effect of field reversal on ion orbit loss was also simulated using the already mentioned ASCOT code [14,16]. The pedestal and SOL plasma profiles were taken for the fwd-B shot 50401 (2.5MA/2.4T, 12 MW NBI), which has previously been modelled extensively and has the same field, current as the 50379/59691 pair, and similar heating power. Self-consistent simulations were performed with a 15 mm-omp pedestal width, equivalent to  $2.5\rho_{\theta i}$  at the outer mid-plane, with  $T_{i,ped} \sim 1.1$  keV and  $T_{i,sep} \sim 400$  eV. Three values of  $E_{r,SOL}$  were used: 0, 45 and 75 kV/m; only the largest field value yields ion peak powers  $> 5$  MW/m<sup>2</sup> as measured for this shot. The results are shown in Fig.6. The effect of field reversal on target power profiles is quite dramatic, with the outer profiles drastically broadened and peak values reduced, in contrast to experiment where little change in  $\lambda_q$  was observed, Fig.3. We are thus forced to conclude that orbit loss is *not* directly responsible for the observed target profiles. More likely, IOL carries power down the pedestal gradient and into the SOL, where (neo-)classical collisional transport takes over.

### 3. ELM transport

Edge localised modes (ELMs) are an integral feature of the H-mode regime. Type-I ELMs originate due to an interaction of two MHD modes: the peeling mode driven by the shear in plasma current and the ballooning mode driven by the pressure gradient [22]. The related MHD activity is strongest on the bad curvature (LFS) side of the plasma. The ELM event results in a rapid drop in density and temperature of the edge plasma 'pedestal' extending up to 20 % of the minor radius beyond the separatrix. This occurs on local Alfvénic and/or sonic time scales, which are comparable to typical SOL transport time scales, i.e.  $L_{\parallel} / c_s \sim 100 \mu s$ . During the ELM crash, the pedestal plasma energy is transported by  $\parallel$ ,  $\wedge$  and  $\perp$  processes to the divertor and limiter tiles. As before,  $\parallel$  and  $\wedge$  mechanisms are largely classical, in this case dominated by kinetic effects in the nearly collisionless ELM filaments, eg. transient sheath formation on open field lines. The ELM filaments propagate radially ( $\perp$ ) on the same timescale with potential consequences for ITER. Mitigating the effects of ELMs poses one of the most pressing problems in tokamak plasma physics.

In order to investigate radial ELM propagation, experiments were carried out focussing on the Langmuir probes located on the outboard limiters, Fig.7, which also shows visible spectroscopy lines of sight (horizontal, vertical, outer and inner divertor), magnetic coils, soft X-ray chords and a 'high-clearance' magnetic equilibrium (near the top of the vertical sweep) used in this study [8]

The chronology of the ELM crash is shown in Fig.8. The MHD activity is quickly ( $< 30 \mu s$ ) followed by a soft X-ray burst (signalling hot electrons striking the inner target), and the rise of the plasma flux (vertical  $D_{\alpha}$ ). The peak of the plasma flux arrives with a delay of  $125 \pm 70 \mu s$  based on the fast signal and  $155 \pm 120 \mu s$  based on the slow signal. The delay of the plasma (ion) pulse with respect to the onset of MHD activity is consistent with the parallel transit time  $\tau_{\parallel} \sim \tau_i \sim L_{\parallel} / \langle Mc_s \rangle \sim 100\text{-}200 \mu s$  for  $M \sim 1$ ,  $L_{\parallel} \sim 30$  m and  $T_i \sim 0.3\text{-}1$  keV ( $\tau_{\parallel}$  evaluated using as a logarithmic average over  $T_i \sim 750$  -

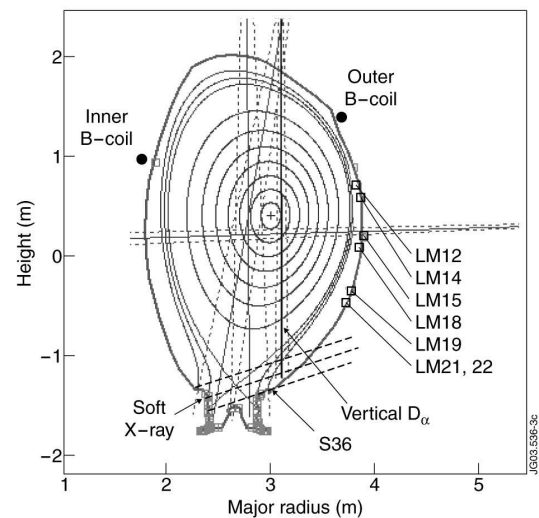


Figure 7: Diagnostics for ELM propagation

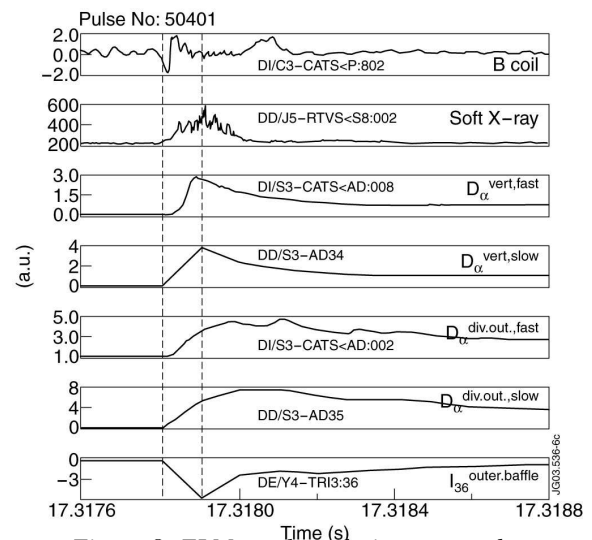


Figure 8: ELM crash evolution as seen by magnetics, target soft X-ray,  $D_{\alpha}$  and probes

250 eV and  $T_e \sim 750 - 25$  eV gives  $\sim 170 \mu\text{s}$ ), Fig.9. The prompt burst of energetic electrons is consistent with the shorter electron transit time  $\tau_{||e} \sim L_{||} / v_e \sim 3-10 \mu\text{s}$  for  $T_e \sim 0.1-1$  keV, Fig.9. The ELM electron temperature at the limiter, estimated using the statistical analysis of the current-voltage spectrum, yields  $T_e^{lim} \sim 25 \pm 5$  eV, independent of location  $r$  or the ELM size  $D_\alpha$ . This is consistent with  $T_e \sim 30$  eV predicted from Fig.9 based on the requirement that  $\tau_{||e} \sim \tau_\perp$ . Unfortunately, Langmuir probes provide no information about the ion temperature of the ELM.

Several hundred ELMs were analysed from twelve identical Type-I H-mode plasmas (2.5 MA, 2.4T), differing only in the amount of plasma heating (10-16 MW),  $D_2$  gas fuelling ( $<1.3 \times 10^{22}$  e/s) and equilibrium position; typically  $f_{ELM} \sim 20-30$  Hz and fractional energy loss per ELM, is in the ITER-relevant range  $\Delta W/W_{ped} \sim 3-5$  %. All discharges were performed on the same day, thus minimising machine conditioning effects. The average peak delay is found to increase linearly with  $\langle r \rangle$ , yielding a radial velocity in the limiter shadow of  $v_\perp^{lim} \sim 0.93 \pm 0.2$  km/s. With the definition  $\Delta t_{\alpha-n} \equiv t_n - t_\alpha \sim \tau_\perp - \tau_{||}$ , the radial propagation time in the SOL may be estimated as

$$\tau_\perp \sim \tau_{||} + \Delta t^{max} \sim 170 + 50 \mu\text{s}, \quad \therefore \xi \sim \frac{\tau_\perp}{\tau_{||}} \sim 1.3 \quad (7)$$

where  $\Delta t^{max}$  is evaluated at the probe closest to the separatrix, at  $r_{lim} \sim 9$  cm. This yields an average propagation velocity in the SOL of  $\langle v_\perp \rangle \sim r_{lim} / \tau_\perp \sim 0.42 \pm 0.2$  km/s, a factor of two lower than the limiter shadow value. Alternatively, if the measured  $\tau_{||} \sim 125 \pm 70 \mu\text{s}$  is used, one obtains  $\langle v_\perp \rangle \sim 0.72 \pm 0.4$  km/s. Both these values are consistent with recent measurements of using the reciprocating probe on JET (shots 51112-7, 2.3 MA, 2.6 T, 13 MW,  $2 \times 10^{19} \text{ m}^{-3}$ ), which indicate radial ELM velocities in the SOL of  $\sim 0.75$  km/s [17]. Averaged over the SOL this yields velocities well below the sound speed,  $\langle v_\perp \rangle / \langle c_s \rangle \sim 0.25-0.4$  %.

The duration of the current signal, as measured by the full-width at half-maximum  $\Delta t^{FWHM}$ , is found to increase roughly as the square root of  $\langle r \rangle$ , which yields an effective diffusivity and the initial width of the ELM pulse,

$$\sqrt{\frac{D_\perp^{lim}}{v_\perp^{lim}}} \sim (0.78 \pm 0.2) v_\perp^{lim} \quad \therefore D_\perp^{lim} \sim 500 \pm 100 \text{ m}^2/\text{s} \quad (8)$$

$$\Delta t_0^{FWHM} = 185 \pm 50 \mu\text{s}, \quad \Delta r_0^{FWHM} \sim \langle v_\perp \rangle \Delta t_0^{FWHM} \sim 8 \pm 2 \text{ cm}$$

The diffusion coefficient is significantly larger than the inter-ELM value, while the initial ELM pulse  $\Delta t_0^{FWHM}$  is comparable to both the radial and parallel propagation times, as well as the duration of edge MHD activity. The radial extent of the ELM, estimated using the Taylor approximation as the distance travelled at  $\langle v_\perp \rangle$  during  $\Delta t_0^{FWHM}$  is thus comparable to the average distance from the separatrix to the limiter,  $r_{lim} \sim 9$  cm.

The simplest model of radial ELM propagation involves the Green's function of the dynamical equations, which describes the transient response to a delta-function impulse,  $f(t) = \delta(t)$ . This is easily found as a advected, gaussian wave-packet,

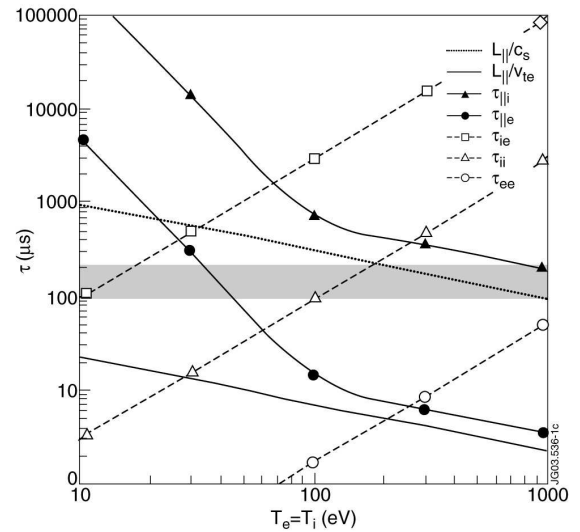


Figure 9: Typical SOL transport times

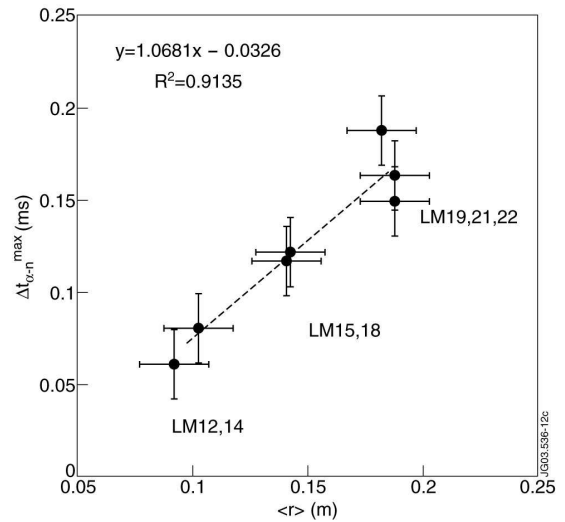


Figure 10: ELM arrival time vs. distance

$$G(t, r) = \frac{1}{\sqrt{\pi \cdot D_{\perp} t}} \exp\left(-\frac{(r - v_{\perp} t)^2}{D_{\perp} t} - \frac{t}{\tau_{\parallel}}\right) \quad (9)$$

which broadens with time as  $(D_{\perp} t)^{1/2}$  while travelling radially with velocity  $v_{\perp}$ . Its maximum decays radially as a reduced-exponential, while its integral is reduced only by parallel losses. The fraction of particles which reach the limiter at  $r = r_{lim}$  decays exponentially with

$$\xi \equiv \int_0^{\tau_{\perp}} \frac{dt}{\tau_{\parallel}} = \int_0^{r_{lim}} \frac{v_{\parallel}}{v_{\perp}} \cdot \frac{dr}{L_{\parallel}} \sim \frac{r_{lim}}{\lambda_n}, \quad \lambda_n \sim L_{\parallel} \left\langle \frac{v_{\perp}}{c_s} \right\rangle \quad (10)$$

Similar results could be derived for the transient energy (E) and temperature (T) evolution by affecting a substitution:  $\chi_{\eta} \rightarrow D_{\eta}$ ,  $\tau_{\parallel\sigma} \rightarrow \tau_{\parallel}$ . Based on Fig.9, we expect the electrons to cool rapidly until  $\tau_{\parallel e}$  approaches  $\tau_{\perp}$ , which occurs at  $T_e \sim 30$  eV, while both the ion temperature and plasmoid density change by roughly one exponential decay length,  $T_i(r)/T_i(0) \sim N(r)/N(0) \sim 1/3$ . Kinetic refinements to the radial decay of particles, energy and temperature of the ELM plasmoid are shown in Fig.11. The plasmoid is cooled as it moves radially, since faster ions are removed preferentially, that is  $T_i \propto E/N$ . For  $\xi \sim 1$ ,  $N/N_0 \sim 0.85$ ,  $E/E_0 \sim 0.42$  and  $T_i/T_{i0} \sim 0.5$ .

A rough estimate of the ELM radial velocity in the SOL may be found via a sheath resistivity plasmoid propagation model, in which  $\mathbf{B} \times \nabla p$  (charge polarisation) and  $\mathbf{E} \times \mathbf{B}$  drifts acting within the ELM filament provide the  $\perp$  drive mechanism. To first order, density reduction by parallel losses and deformation/break-up by vorticity effects set upper and lower limits on the plasmoid size, and hence lower and upper limits on the radial velocity [18],

$$\frac{v_{\perp}^{\min}}{c_s} = \left(\frac{\rho_i}{R}\right)^{2/3} \left(\frac{L_{\parallel}}{R}\right)^{-1/3}, \quad \frac{\delta^{\max}}{\rho_i} = \left(\frac{\rho_i}{R}\right)^{-1/3} \left(\frac{L_{\parallel}}{R}\right)^{2/3}$$

$$\frac{v_{\perp}^{\max}}{c_s} = \left(\frac{\rho_i}{R}\right)^{2/5} \left(\frac{L_{\parallel}}{R}\right)^{-1/5}, \quad \frac{\delta^{\min}}{\rho_i} = \left(\frac{\rho_i}{R}\right)^{-1/5} \left(\frac{L_{\parallel}}{R}\right)^{2/5} \quad (11)$$

For typical initial conditions at the outer mid-plane during Type-I ELMs on JET ( $T_i = T_e \sim 500$  eV;  $B_t \sim 2.0$  T;  $L_{\parallel}/R \sim 10$ ;  $D^+$  ions) this yields,

$$3 \times 10^{-3} < v_{\perp}/c_s < 3 \times 10^{-2}, \quad c_s \sim 200 \text{ km/s} \quad (12)$$

$$10 < \delta/\rho_i < 50, \quad \rho_i \sim 2 \text{ mm}$$

According to this theory, we would expect formation of Type-I ELM filaments of several cm poloidal extent, propagating radially with velocities on the order of a km/s, leading to radial SOL transit times of  $\sim 100 \mu\text{s}$ . This is quantified in Fig.12, where the predictions of the lower and upper bounds of the sheath limited model (11) are compared with JET measurements ( $\langle v_{\perp} \rangle \sim 0.45\text{-}0.75$  km/s or  $\langle v_{\perp} \rangle / \langle c_s \rangle \sim 0.25\text{-}0.4$  %) represented by the two shaded regions in Fig.12. The experimental data result is well matched by the lower bound (set by  $\parallel$  losses) of the sheath-limited model (11). The predicted size of the initial filaments is consistent with the observation of toroidal mode numbers  $> 10$  on AUG [19].

Using the above velocity to relate the filament radial position and time, the radial ELM decay lengths of density and electron temperatures are inferred as  $\lambda_n^{\text{ELM}} \sim 12 \pm 2$  cm and  $\lambda_{T_e}^{\text{ELM}} \sim 3 \pm 1$  cm, respectively (the less than or equal signs entering due to kinetic corrections, Fig.11, in light of the point measurements of ELM  $n_e$  and  $T_e$ ). Although ion temperature is not measured directly, power

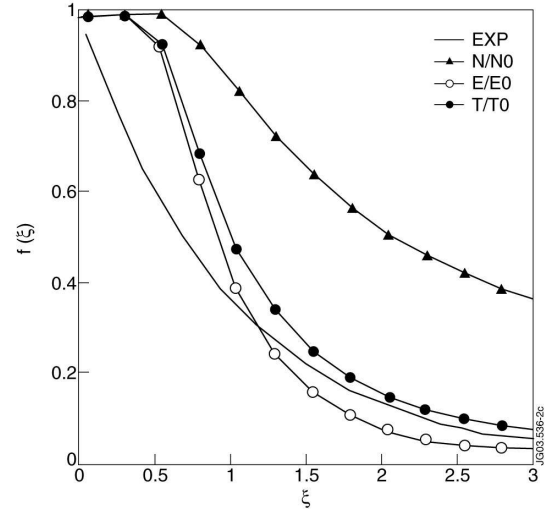


Figure 11: Kinetic estimates of radial decays of particles and energy in the ELM filament

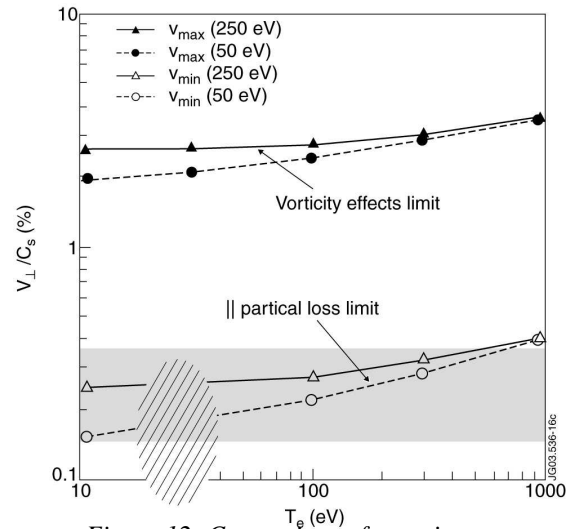


Figure 12: Comparison of experiment vs. sheath limited plasmoid propagation theory

balance measurements suggest  $\lambda_{Ti}^{ELM} \sim 8 \pm 2$  cm, which would imply that much more ion than electron energy reaches the outboard limiters as a result of the ELM burst. This prediction is supported by a) simple kinetic predictions in the frame of reference of the ELM filament, Fig.9&11, b) first results from a generalised model of plasma transients, which suggests  $T_i/T_e > 3$  at  $t = \tau_{\parallel s} \sim L_{\parallel}/c_s$  for a typical JET ELM filament at the limiter location, c) preliminary analysis of retarding field analyser data which indicates ion energies during the ELM burst characteristic of the ion pedestal temperatures. We expect radial sweep experiments to provide an improved estimate of the ELM ion energy.

#### 4. Conclusions and Implications for ITER

Significant progress has been made in understanding the energy transport mechanisms in the SOL under ITER-relevant conditions. Analysis of measured divertor power profiles suggests  $\parallel$  energy transport in the near-SOL to be largely classical (plus kinetic effects such as gyro-viscosity, heat flux limits, sheath formation, etc.),  $\wedge$  energy transport to be governed by classical drifts (primarily  $\mathbf{E} \times \mathbf{B}$  and  $\mathbf{B} \times \nabla p$ ),  $\perp$  electron energy transport to be dominated by interchange MHD and drift-wave turbulence, and  $\perp$  ion energy transport (the dominant channel) to be dominated by (neo-)classical ion conduction. The co-existence of turbulent (electrons) and collisional (ions) transport can be understood in terms of the much larger dissipative scale for ion, than for electron, thermal energy losses (direct consequence of the larger ion gyro-radius). Neo-classical ion orbit loss likely determines the  $\perp$  ion power flow into the SOL where collisional processes take over. Extrapolating to ITER, using expected separatrix values of  $n_{e,sep} = 3 \times 10^{19} \text{ m}^{-3}$  and  $2T_{e,sep} = T_{i,sep} = 400 \text{ eV}$  ( $v_{i,sep}^* = 1.1$ ), we find an integral power width of  $\lambda_q^{ITER} \sim 3.7 \pm 1.1$  mm at the entrance into the divertor throat, below the design value of 5 mm. We expect this profile to be broadened by charge-exchange collisions in the dense ITER divertor.

Limiter Langmuir probe data indicates significant ELM interaction with the outboard limiters on JET. Radial propagation velocities of the ELM filaments have been measured as  $\langle v_{\perp} \rangle \sim 0.6 \pm 0.3$  km/s,  $\langle v_{\perp} \rangle / \langle c_s \rangle \sim 0.3 \pm 0.1$  % and  $\langle v_{\perp} / c_s \rangle \sim 0.2$  % in fair agreement with other machines (DIII-D, C-mod, MAST)[21] and JET reciprocating probe data [17]. These velocities are well explained via a simple propagation model in which classical drifts (diamagnetic  $\mathbf{B} \times \nabla p$  and  $\mathbf{E} \times \mathbf{B}$ ) and sheath resistivity provide the driving mechanism. While the electron energy is rapidly lost from the ELM filament by parallel losses, the ion energy is removed on the slower dynamical time scale,  $\tau_{\parallel s} \sim L_{\parallel}/c_s$ ; kinetic modelling predicts  $T_i/T_e > 3$  at  $t = \tau_{\parallel s}$ , such that most of the power deposited at the limiter would come from the ions. Extrapolating to ITER, we expect up to  $4 \pm 1$  % of the electron and  $13 \pm 3$  % of the ion ELM energy to reach the outboard beryllium limiter, situated 5 cm beyond the separatrix. Taking the initial conditions of the ELM filament at half the pedestal values, yields the peak values at the ITER limiter:  $n_e \sim 3.0 \times 10^{19} \text{ m}^{-3}$ ,  $T_i \sim 2.5T_e \sim 1.0 \pm 0.2 \text{ keV}$ . On the evidence of *toroidally* asymmetric structure of ELMs observed on AUG [19] and MAST [20], we expect the associated energy fluxes to be *poloidally* localised on the limiter, with resulting power loads above those envisioned in the original ITER design.

*This work was conducted under European Fusion Development Agreement and was partly funded by EURATOM and the United Kingdom Engineering and Physical Sciences Research Council.*

- [1] G.Federici et al., *Nuclear Fusion* **41** (2001) 1967. [2] ITER Physics Basis, *Nuclear Fusion* **39** (1999) 2391-2469 (Chapter 4). [3] G.F.Matthews et al., *Nuclear Fusion*, **43** (2003) 999. [4] V.Riccardo et al., *Plasma Physics and Controlled Fusion*, **43** (2001) 881. [5] W.Fundamenski et al., *J. Nucl. Mat.*, **290** (2001) 593. [6] W.Fundamenski et al., *J. Nucl. Mat.*, **313** (2003) 787. [7] W.Fundamenski et al., *Plasma Phys. Contr. Fusion*, **44** (2002) 761. [8] W.Fundamenski et al., *Plasma Phys. Control. Fusion*, **46** (2004) 233. [9] W.Fundamenski et al., *Nuclear Fusion*, **44** (2004) 20. [10] W.Fundamenski, *11<sup>th</sup> European Fusion Physics Workshop, Heraklion, Crete* (dec.2003). [11] Y Andrew et al., *Plasma Phys. Control. Fusion* **46** (2004) 337. [12] J.-W. Kim et al, *J. Nucl. Mat.*, **290** (2001) 644. [13] R.A.Pitts et al., *J. Nucl. Mat.*, in press. [14] W.Fundamenski et al., *J. Nucl. Mat.*, in press. [15] A.Chankin, *J. Nucl. Mat.*, **241-243** (1997), 199. [16] J.A.Heikkinen et al., *Phys. Plasmas*, **8** (2001), 2824. [17] B.Goncalves et al., *Plasma Phys. Control. Fusion* **45** (2003) 1627. [18] S.I.Krashennnikov, *Physics Letters A*, **283** (2001) 368. [19] T.Eich et al., *Phys. Rev. Lett.*, **91** (2003) 195003. [20] A.Kirk et al., *Phys. Rev. Lett.*, **92** (2004) 245002. [21] J. Boedo et al., *J. Nucl. Mat.*, in press. [22] A.Becoulet et al., *Plasma Phys. Control. Fusion* **45** (2003) A93.